

Strong lensing constraints on primordial black holes as a dark matter candidate

Veronica Dike¹,^{*} Daniel Gilman² and Tommaso Treu¹

¹*Department of Physics and Astronomy, University of California Los Angeles, Los Angeles, CA 90095, USA*

²*Department of Astronomy and Astrophysics, University of Toronto, 50 Saint George Street, Toronto, ON M5S 3H4, Canada*

Accepted 2023 April 18. Received 2023 April 11; in original form 2022 October 15

ABSTRACT

Dark matter could comprise, at least in part, primordial black holes (PBHs). To test this hypothesis, we present an approach to constrain the PBH mass (M_{PBH}) and mass fraction (f_{PBH}) from the flux ratios of quadruply imaged quasars. Our approach uses an approximate Bayesian computation forward modelling technique to directly sample the posterior distribution of M_{PBH} and f_{PBH} , while marginalizing over the subhalo mass function amplitude, spatial distribution, and the size of the lensed source. We apply our method to 11 quadruply imaged quasars and derive a new constraint on the intermediate-mass area of PBH parameter space $10^4 M_{\odot} < M_{\text{PBH}} < 10^6 M_{\odot}$. We obtain an upper limit $f_{\text{PBH}} < 0.17$ (95 per cent confidence limit). This constraint is independent of all other previously published limits.

Key words: gravitational lensing; strong – dark matter.

1 INTRODUCTION

Primordial black holes (PBHs) are an appealing dark matter (DM) candidate because they do not require physics beyond the standard model and black holes are known to exist in nature. In the early Universe, overdensities could have created the earliest black holes (Zel'dovich & Novikov 1967; Hawking 1971), and these black holes could persist into the present day to make up part or all of the DM in the Universe (Carr & Hawking 1974; Chapline 1975). For a recent overview of PBHs as a DM candidate, see Carr & Kühnel (2020) and Green & Kavanagh (2021). Narrowing the PBH parameter space can place constraints on various models of cosmological significance because PBH formation and evolution is entwined with the history of the Universe.

The hypothetical parameter space for PBHs is very wide. Their mass distribution is virtually unconstrained theoretically, and they do not necessarily have to account for the entirety of DM. Observations exclude many mass ranges for PBHs representing 100 per cent of DM, but the constraints are much weaker for a population that makes up only a fraction of DM (see e.g. Belotsky et al. 2019; Carr et al. 2021). For black holes of mass M_{PBH} greater than $10^2 M_{\odot}$, fast radio burst lensing constrains the fraction of DM in PBH, f_{PBH} , to less than 9 per cent (Zhou et al. 2022a). PBH as all DM requires a population of around subsolar mass, but is consistent with the fast radio burst rate in the model of Kainulainen et al. (2021). A stellar-mass-scale PBH distribution is detectable as microlensing in strongly lensed quasars, in cases where microlensing by stars can be suppressed (Hawkins 2020).

Carr et al. (2021) put forward a multi-peaked PBH mass function (including a high-mass peak of $10^6 M_{\odot}$) that could explain a range

of phenomena from cosmic infrared background excess to black hole merger rates. See also Khlopov (2010) for an overview of cosmological implications of PBH formation mechanisms. PBH non-detection can itself constrain the scale of isocurvature perturbations in cold DM (CDM) in the early Universe (Passaglia & Sasaki 2022). A small DM fraction of high-mass PBH could seed supermassive black holes and galaxy formation (Carr & Silk 2018), and in turn the observed population of supermassive black holes can also be used to constrain the PBH mass function (Cai et al. 2023).

A powerful and direct way to probe the PBH contribution to DM is strong gravitational lensing (see e.g. Treu 2010, and references therein). Intrinsically point masses, PBHs are particularly effective deflectors. Their observational signature depends only on their mass, with the deflection angle in terms of impact parameter ξ modelled as $\alpha = 4GMc^{-2}\xi^{-1}$. The method of gravitational imaging (Koopmans 2005; Vegetti et al. 2010; He et al. 2022) could in principle be used to detect individual PBHs of masses greater than $10^3 M_{\odot}$ (Banik et al. 2019), and lensing constraints from compact radio sources can also be used to constrain high-mass PBHs (Zhou et al. 2022b). Because constraints from lensing are completely independent of others that have been used to constrain PBHs in a similar mass range, such as dynamical constraints (Carr & Sakellariadou 1999; Quinn et al. 2009; Brandt 2016), X-ray background constraints on accretion rate (Inoue & Kusenko 2017), or Lyman- α forest enhancement constraints (Afshordi, McDonald & Spergel 2003; Mack, Ostriker & Ricotti 2007; Murgia et al. 2019), lensing provides a vital cross-check.

Anomalies in the ratios of flux between images of the same lensed source can reveal substructure in the lensing mass distribution. This technique, suggested initially by Mao & Schneider (1998), can probe structure at lower mass scales than those accessible with gravitational imaging. Such flux ratio anomaly studies rely on observations of lensed sources that are large enough to avoid being affected by

* E-mail: veronica.j.dike@gmail.com

Table 1. Priors for the parameters in our model that are lens-dependent. For a description of all free parameters, including those with priors shared between all lenses, see text. The host halo mass M_{host} has a Gaussian prior and other priors are uniformly distributed. The rightmost column has the reference for the photometry data.

Lens name	σ_{source} (pc)	M_{host} (M_{\odot}) (μ, σ)	γ_{ext}	Ref.
B1422+231	25–60	13.3, 0.3	0.08–0.4	Nierenberg et al. (2014)
HE0435–1223	25–60	13.2, 0.3	0.015–0.15	Nierenberg et al. (2017)
MG0414+0513	5–15	13.5, 0.3	0.01–0.32	Stacey & McKean (2018) and Stacey, Lafontaine & McKean (2020)
PG 1115+080	5–10	13.0, 0.3	0.002–0.12	Chiba et al. (2005)
PS J1606–2333	25–60	13.3, 0.3	0.1–0.28	Nierenberg et al. (2020)
RX J0911+0551	25–60	13.1, 0.3	0.05–0.25	Nierenberg et al. (2020)
RX J1131–1231	25–80	13.9, 0.3	0.06–0.28	Sugai et al. (2007)
WFI 2026–4536	25–60	13.3, 0.3	0.015–0.16	Nierenberg et al. (2020)
WFI 2033–4723	25–60	13.3, 0.3	0.07–0.26	Nierenberg et al. (2020)
WGD J0405–3308	25–60	13.3, 0.3	0.0025–0.12	Nierenberg et al. (2020)
WGD 2038–4008	25–60	13.04, 0.15 ^a	0.005–0.08	Nierenberg et al. (2020)

Note. ^aThis value is from Shajib et al. (2022).

stellar microlensing; see Dobler & Keeton (2006) for an analysis of the effect of source size on flux ratio analysis. Examples of such sources include radio emission in radio-loud quasars (Mao & Schneider 1998; Metcalf & Madau 2001; Dalal & Kochanek 2002; Hsueh et al. 2020), mid-infrared emission from the hot dust in active galactic nuclei (AGNs; Chiba et al. 2005), and the narrow-line region of AGNs (Moustakas & Metcalf 2003; Nierenberg et al. 2014, 2017, 2020).

Gilman et al. (2020a, b) presented an analysis framework that uses the flux ratios among images in quadruply imaged quasars (quads) to constrain the properties of DM structure in strong lens systems. These techniques can be adapted to constrain a variety of DM models, including CDM, warm DM (Gilman et al. 2020a), self-interacting DM (Gilman, Zhong & Bovy 2023), and fuzzy DM (Laroche et al. 2022), given a prescription for the halo mass function and density profiles of haloes.

In this paper, we present new constraints on the PBH parameter space by analysing the flux ratio anomalies in a sample of strongly lensed quasars observed in the narrow-line regime (Nierenberg et al. 2014, 2017, 2020). In Section 2, we explain our method of sampling the posterior distribution of our PBH parameters of interest using forward modelling. In Section 3, we present the results of our modelling and comparison to real data, and in Section 4 we discuss further expansions on this study. When necessary, we use the cosmology parameters of Planck Collaboration VI (2020) throughout this analysis, although we stress that our results do not depend sensitively on this assumption.

2 METHODS

In this section, we first describe the goal of this paper, to obtain a posterior distribution on the PBH parameters of interest, which we achieve using an approximate Bayesian computation (ABC) forward modelling method. We first model the lens substructure using the method developed in Gilman et al. (2019), and then we model the effect of a possible PBH population.

2.1 Inference

We are striving to measure the posterior probability of DM model parameters; here, our likelihood function \mathcal{L} can be written as

$$\mathcal{L}(D_i|\theta_{f,M}) = \int p(D_i|m_r, \theta_r) p(\theta_r, m_r|\theta_{f,M}) dm_r d\theta_r, \quad (1)$$

where D_i refers to the observed image positions and flux ratios for a certain lens, $\theta_{f,M}$ represents our target model parameters, M_{PBH} and f_{PBH} , m_r is a certain lens model realization, and θ_r is the set of non-PBH model parameters that we marginalize over. We use the method described by Gilman et al. (2020a) to sidestep evaluating this integral directly, which would require a computationally intractable exploration of a vast parameter space. This sidestepping is accomplished by forward modelling data, generating flux ratios from many sets of model parameters, and then comparing the results to the observed data via a summary statistic; from this process, we can extract $\theta_{f,M}$ that represents our posterior probability distribution. This is an ABC method (Rubin 1984, see also, e.g. Sisson, Fan & Beaumont 2018) of creating a large set of stochastically varying simulated data and accepting simulations close to the real data to sample a posterior. ABC has been used in astrophysical forward modelling problems where a direct calculation of the likelihood function is infeasible and data can be simulated (see e.g. Weyant, Schafer & Wood-Vasey 2013; Akeret et al. 2015; Birrer, Amara & Refregier 2017).

We use the sample of 11 quads selected for flux ratio analysis by Gilman et al. (2022, section 2.2) because the size of the source, either observed as [O III] emission from the narrow-line region or CO (10–11) radio emission, is larger than the scale that would be affected by microlensing or image arrival time delay, and the main lensing galaxy does not require modelling for a known stellar disc component (Hsueh et al. 2016, 2017; Gilman et al. 2017). Photometry data used for each lens are referenced in Table 1.

We generate a lens model using LENSTRONOMY¹ (Birrer & Amara 2018; Birrer et al. 2021). The lens model is optimized to match the observed image position, with the added astrometric uncertainty. Any draw of parameters that does not match the observed image positions would be rejected in the posterior, so we reduce computation time by requiring the lens model fit the positions.

We compute the magnification, and thus the flux, of each image in our lens system model realization, then obtain the three flux ratios r_{model} between the four images. Only flux ratios are used because the intrinsic source brightness is not known. We compare the forward-modelled flux ratios to the observed flux ratios r_{obs} with the summary statistic

$$S(r_{\text{model}}, r_{\text{obs}}) = \sqrt{\sum_{i=1}^3 (r_{\text{model}(i)} - r_{\text{obs}(i)})^2}. \quad (2)$$

¹<https://github.com/sibirrer/lenstronomy>.

We generate $\mathcal{O}10^5\text{--}10^6$ lens model realizations sampling from our parameter space from which we choose the 1500 lowest summary statistics to represent a sample of the posterior distribution. We construct a continuous approximation of the likelihood function for each lens by applying a kernel density estimate to the accepted samples, and multiply the resulting likelihoods to obtain the final posterior.

2.2 Model parameters

The lens and halo substructure modelling process follows from Gilman et al. (2019, 2020a, b). The lensing galaxy, or main deflector, is modelled as a power-law ellipsoid with external shear. The properties of the main deflector that are optimized during initial lens model fitting are the Einstein radius, centroid, ellipticity, ellipticity angle, and shear angle. If the main deflector has any known satellite galaxies, they are included in the model as a singular isothermal sphere mass profile. The main deflector mass M_{host} , log profile slope γ_{macro} , and shear γ_{ext} are sampled in the forward model.

Subhaloes are rendered from 10^6 to $10^{10} M_{\odot}$, from the lowest mass we are sensitive to to the highest mass of halo we expect to be entirely DM. The projected mass density Σ_{sub} and power-law slope α parametrize the subhalo mass function (SHMF),

$$\frac{d^2 N_{\text{sub}}}{dm dA} = \frac{\Sigma_{\text{sub}}}{m_0} \left(\frac{m}{m_0}\right)^{\alpha} \mathcal{F}(M_{\text{halo}}, z), \quad (3)$$

where $\mathcal{F}(M_{\text{halo}}, z)$ is a function to scale the number density of subhaloes with main lensing halo mass and redshift as described in Gilman et al. (2020a). The pivot mass m_0 is set to $10^8 M_{\odot}$ (Fiacconi et al. 2016). For the line-of-sight haloes, we use the Sheth–Tormen halo mass function (Sheth, Mo & Tormen 2001) with two-halo term $\xi_{2\text{halo}}$ as a scaling factor to account for correlated structure near the host halo (see Gilman et al. 2019) and δ_{los} as an overall amplitude scaling factor:

$$\frac{d^2 N_{\text{los}}}{dm dV} = \delta_{\text{los}} (1 + \xi_{2\text{halo}}(M_{\text{halo}}, z)) \left. \frac{d^2 N}{dm dV} \right|_{\text{Sheth-Tormen}}. \quad (4)$$

Given the PBH mass is distributed along with CDM subhaloes, the Sheth–Tormen mass function should be broadly applicable, but there may be an enhancement of the power spectrum on small scales caused by isocurvature perturbations from PBH (Afshordi et al. 2003; Gong & Kitajima 2017). Our constraint is more conservative because we do not take this enhancement into account. The free model parameters and priors are as follows:

(i) $M_{\text{PBH}} (M_{\odot})$, the PBH monochromatic mass, with a prior of 10^4 to $10^6 M_{\odot}$ chosen to include PBHs that are large enough to affect the flux ratios given the background source size but not larger than the minimum rendered halo mass;

(ii) f_{PBH} , the PBH mass fraction of total DM, with a prior of 0–50 per cent;

(iii) Σ_{sub} , the SHMF normalization, with a prior of 0–0.1 kpc^{-2} . We allow broad uncertainty in the number of subhaloes to account for uncertainties associated with tidal stripping;

(iv) α , the log slope of SHMF, with a prior ranging from -1.85 to -1.95 as predicted by Lambda CDM N -body simulations (Springel et al. 2008, Fiacconi et al. 2016);

(v) δ_{los} , the line-of-sight halo mass function scaling factor, with a prior of 0.8–1.2 that accounts for differences between theoretical models of the halo mass function (e.g. Despali et al. 2016) and uncertainties in cosmological parameters;

(vi) γ_{macro} , the log slope of main deflector mass profile, with a data-motivated prior of 1.9–2.2 (Auger et al. 2010);

(vii) σ_{source} , the background source size, differing depending on whether the source is observed in narrow-line (Müller-Sánchez et al. 2011) or other regions (Chiba et al. 2005; Stacey et al. 2020) surrounding the background quasar listed for each lens in Table 1;

(viii) M_{host} , the mass of the main lens host galaxy [see Table 1 and Gilman et al. (2020a) for a discussion of these priors constructed from individual lens data];

(ix) γ_{ext} , the external shear in the main lens plane [see Table 1, with ranges based on the individual lens data determined in Gilman et al. (2022)];

(x) δ_{xy} (mas), the image position uncertainty;

(xi) δ_f , the image flux uncertainty.

References to photometric measurement information are listed in Table 1. Our target parameters are M_{PBH} and f_{PBH} , and we marginalize over the others when they are sampled together in the posterior. For each realization, the model parameters are drawn from a prior distribution and the halo placement is stochastic. Some lenses have photometrically estimated redshifts (Gilman et al. 2020a), so we sample the redshift probability distribution function and marginalize over it for those lenses.

Lens RXJ1131+1231 was modelled with two Gaussian source components to match the data of Sugai et al. (2007). Lenses with an imaged satellite companion are modelled with the companion in the source plane as a single isothermal sphere with position uncertainty of 50 mas.

2.3 PBH deflection modelling

If some fraction f_{PBH} of DM exists in the form of PBHs, the distribution of these objects should follow a population of haloes with Navarro–Frenk–White (NFW) profiles (Navarro, Frenk & White 1997). Thus, the first step in our analysis is to generate a population of NFW haloes and subhaloes throughout the lensing volume. We create a realization of DM haloes and subhaloes using the LENSTRONOMY affiliate package PYHALO² (Gilman et al. 2021). We can calculate the mass fraction of DM rendered in haloes f_{halo} , which we use to determine the number of PBHs that are clustered with the halo mass, and a stochastic distribution of line-of-sight and lens-plane subhalo masses, which we use to determine the clustered PBH position.

To determine the spatial distribution of the black holes at each redshift plane along the line of sight, we first compute the projected mass in DM at the lens plane from the population of NFW haloes distributed throughout the lensing volume. If we were to render haloes down to the minimum halo mass in CDM, then all of the PBHs would track the density of DM in haloes. However, as we only render a fraction of the total mass of DM in haloes, a number $N_{\text{clustered}} = (f_{\text{PBH}})(f_{\text{halo}})(\rho_{\text{DM}}(z))(V/M_{\text{PBH}})$ will track the DM density in haloes. We distribute this population of PBHs with a spatial probability density that varies in proportion with the project mass in DM at each lens plane, as illustrated by Fig. 1. The mass added in PBH is removed from the rendered particle–DM subhalo mass. We place the remaining N_{smooth} point masses randomly across each redshift plane, tracking the smooth background distribution of DM that we do not place in haloes. For each image of the lens, we add PBH at discrete redshift steps along the line of sight within a circular aperture of 0.24 arcsec for $10^8 M_{\odot}$, scaling with the root M_{PBH} to a minimum of 0.15

²<https://github.com/dangilman/pyHalo>.

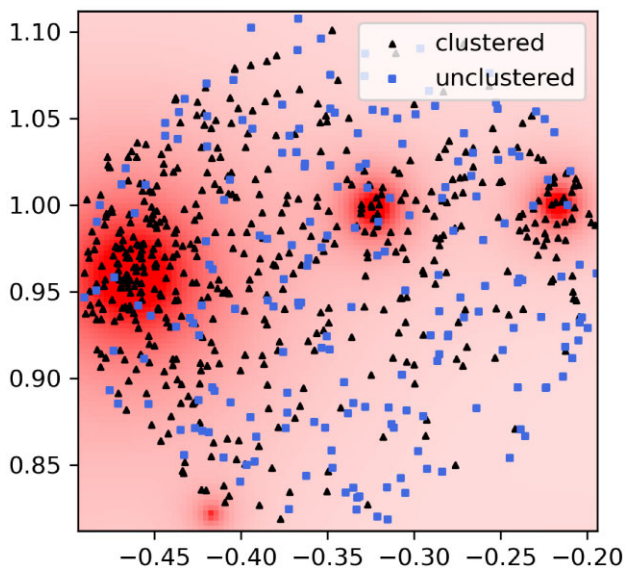


Figure 1. An example of PBH positions in a single lens plane. In this figure, M_{PBH} is $10^4 M_{\odot}$ and f_{PBH} is 0.5. The axes are in arcseconds and the background colourmap intensity varies linearly with the projected mass in DM. The unclustered population (blue squares) is distributed uniformly across the rendering aperture, while the clustered population (black triangles) tracks the projected DM mass density in haloes.

arcsec. For images closer than 0.24 arcsec, we add half the distance between the two points to the aperture and centre it at the mid-point between the images, treating the rendering area for those images as one aperture as illustrated in Fig. 2.

In Fig. 3, we have plotted effective multiplane convergence for a lens model with $M_{\text{PBH}} = 10^{5.5} M_{\odot}$ and $f_{\text{PBH}} = 0.4$ alongside that of a model with no PBH substructure. This effective multiplane convergence is defined as the multiplane convergence (half the divergence of the effective deflection through the lensing planes α_{eff}) from the lens model minus the macromodel convergence, thus $\kappa_{\text{eff}} \equiv \frac{1}{2} \nabla \cdot \alpha_{\text{eff}} - \kappa_{\text{macro}}$. On a convergence map, which corresponds to surface density, the point masses produce markedly different lensing signatures to the less centrally concentrated NFW profiles.

After the PBHs have been distributed in the lens model, the deflection from the new point masses is accounted for by refitting the

lens model to the observed image positions. We raytrace through this final lens model to get the simulated image flux ratios, and calculate our summary statistic for the realization.

3 RESULTS AND COMPARISON WITH PREVIOUS WORK

We present our constraint on PBH DM from the posterior distribution of our target PBH parameters for 11 lenses (in Fig. 4), which were combined and marginalized over the main deflector and subhalo parameters described in Section 2.2. We obtained a 95 per cent upper limit on f_{PBH} of 0.17 across the probed mass range. We see that there is a tentative anticorrelation between M_{PBH} and f_{PBH} , as we would expect.

Our constraint is plotted along with others in the same mass range in Fig. 5. The constraint is stronger than that placed by radial velocity measurements of three wide binary systems that could be disrupted by a PBH population (Quinn et al. 2009), but it is partially within the bounds of the other four constraints. However, our method is totally independent of the other bounds, and thus provides an important cross-check of the assumptions of other methods and their potential systematic uncertainties.

The X-ray accretion background constraint depends sensitively on assumption about the physics of gas accretion on to PBH and the possible subsequent formation of an accretion disc, the density of the interstellar medium (ISM), and PBH motion through the ISM. The constraint shown from Brandt (2016), similar to that of Quinn et al. (2009), is from the survival of the Eridanus II star cluster that would be dynamically heated into dispersal by PBH DM. This assumes that the Eridanus II cluster formed in place. The dynamical constraint placed by Carr & Sakellariadou (1999) assumes that PBHs will drift to the centres of galaxies, but this has been argued to be avoidable if PBHs are regularly dynamically ejected as well (Xu & Ostriker 1994). The LSS constraint in Fig. 5 is from the effect of PBHs on the matter power spectrum as probed by the Lyman- α forest, which in turn depends on assumptions and modelling of its thermodynamics (Viel et al. 2013; Villasenor et al. 2022).

Finally, as shown by Banik & Bovy (2021), N -body simulations with DM particle masses comparable to the PBH mass range we consider result in small-scale perturbations to stellar streams. Interpreting this result in the context of PBHs suggests that streams also can constrain the contribution of PBHs to the DM.

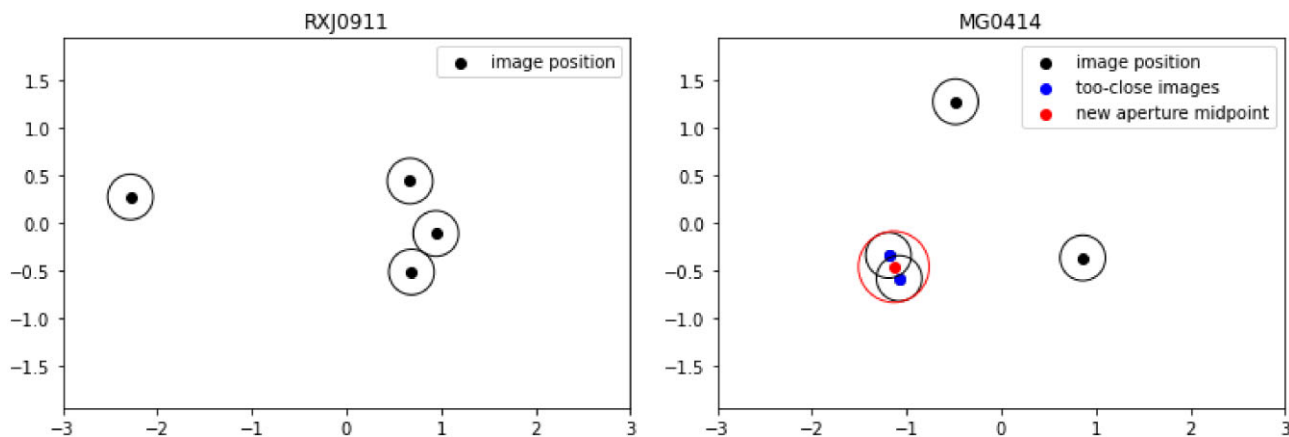


Figure 2. Visualization of rendering area relative to image position. The circles around the image positions represent the rendering area for lensing substructure. On the left, for lens RX J0911+0551, these areas do not overlap for the chosen radius of 0.24 arcsec. On the right, there is significant overlap between the rendering areas for two images, so a new aperture is drawn around both images to avoid double placement of PBH in the overlap region.

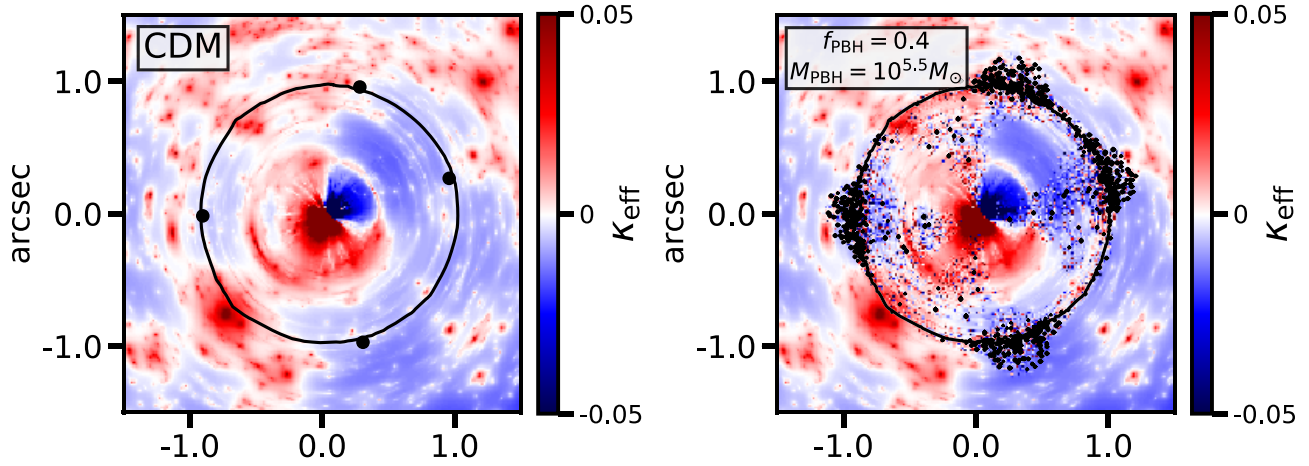


Figure 3. Effective multiplane convergence, a two-dimensional representation of a full population of line-of-sight haloes and subhaloes, for a DM realization in CDM (left) and with PBH substructure (right). Red corresponds to a density higher than that of the mean DM density, while blue corresponds to an underdensity. Black circles are plotted at each of the four quad image positions, and the black curves are the critical curves, which follow the region of maximum image magnification. Small-scale features in the convergence map that appear to track towards the origin are associated with black holes rendered around the path followed by the lensed light rays. Deformation of the critical curve by the PBH population suggests they will strongly perturb image flux ratios.

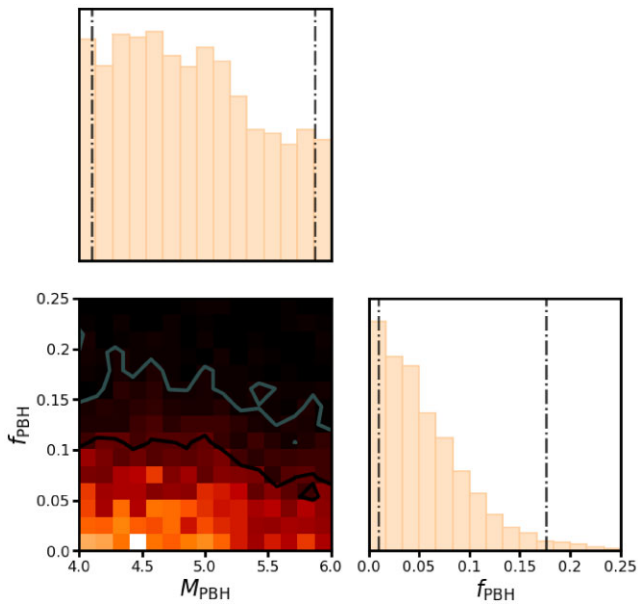


Figure 4. Joint posterior distribution of the PBH mass and mass fraction obtained from analysing 11 strong lenses, marginalized over Σ_{sub} , α , and δ_{los} . The vertical dot-dashed lines in the panels showing marginal likelihoods represent 95 per cent confidence intervals. The lighter contours bound the 95 per cent confidence region and the darker contours bound the 68 per cent confidence region.

4 DISCUSSION AND CONCLUSIONS

We develop a new method for including PBH substructure in a lens model for flux ratio analysis, and present independent constraints on the fraction of DM that could be composed of relatively massive PBHs. We obtained a constraint on f_{PBH} less than 0.17 for $M_{\text{PBH}} = 10^4$ to $10^6 M_{\odot}$ (95 per cent CL). The mass distribution for the PBHs in this work is monochromatic as a conservative constraint, but the limit can be converted to an arbitrary extended mass distribution via the method presented in Carr et al. (2017). This constraint is totally independent of others in the same mass range.

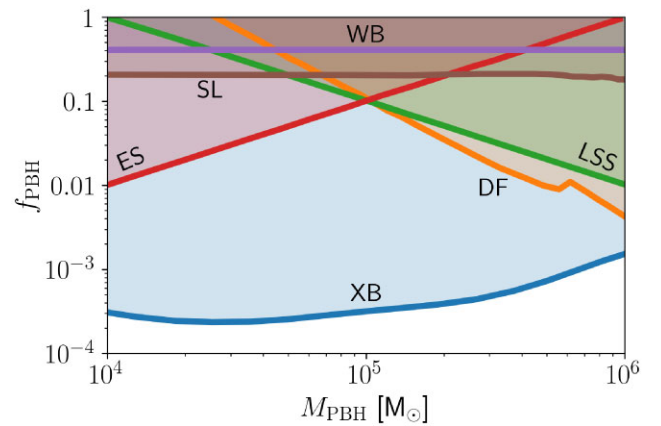


Figure 5. Constraints from disruption of wide binaries (WBs; Quinn et al. 2009), Eridanus II star cluster surviving possible destruction by dynamical heating (ES; Brandt 2016), halo dynamical friction (DF; Carr & Sakellariadou 1999), large-scale structure (LSS; Afshordi et al. 2003; Mack et al. 2007), X-ray background from accretion (XB; Inoue & Kusenko 2017), and our constraint from strong lensing flux ratio analysis (SL).

In the spirit of a first application of this method, we make several simplifying assumptions throughout this process. We do not account for the effect of PBH formation on the assembly history of subhaloes and how that could possibly affect the mass functions and density profiles that we are also assuming. We allow for a very general parametrized form of these functions and marginalize over the parameter space to reduce the rigidity of our models. As samples of quads improve and our method becomes more constraining, we will revisit the simplifying assumptions.

In the future, these constraints will be improved by applying the method to larger samples of lenses that are currently being discovered (Schmidt et al. 2023) and will be discovered in wide field surveys such as the Vera C. Rubin, Euclid, and Roman Observatories (e.g. Oguri & Marshall 2010). Lens systems can also be followed up with adaptive-optics-assisted instruments from the ground (Wright et al. 2019; Wizinowich et al. 2022). Forthcoming data from the *JWST*

(Nierenberg et al. 2021) will allow us to push to lower PBH mass scales because *JWST* will measure flux ratios in the mid-infrared. This emission comes from a more spatially compact ($\sim 1\text{--}10$ pc) region around the background source. The minimum deflection angle that impacts our data is determined by the size of the source, so the more compact source size will allow us to push to lower PBH mass scales than we can currently measure.

ACKNOWLEDGEMENTS

The authors thank Alex Kusenko for insightful and stimulating conversations, and Xiaolong Du for a productive discussion on halo mass functions.

This material is based upon work supported by the National Science Foundation Graduate Research Fellowship Program under grant no. DGE-1650604. Any opinions, findings, and conclusions or recommendations expressed in this material are those of the authors and do not necessarily reflect the views of the National Science Foundation.

VD thanks the Legacy Survey of Space and Time Corporation Data Science Fellowship Program, which is funded by Legacy Survey of Space and Time Corporation, National Science Foundation Cybertraining Grant #1829740, the Brinson Foundation, and the Moore Foundation; her participation in the programme has benefited this work.

DG was partially supported by an Highly Qualified Personell grant from the McDonald Institute (reference number HQP 2019-4-2).

TT acknowledges support by the National Science Foundation through grants NSF-AST-1714953, NST-AST-1836016, and NSF-AST-2205100 and by the Gordon and Betty Moore Foundation through grant 8548.

This work used computational and storage services associated with the Hoffman2 Shared Cluster provided by University of California Los Angeles Institute for Digital Research and Education's Research Technology Group.

This research is based on measurements made with the NASA/ESA *Hubble Space Telescope* obtained from the Space Telescope Science Institute, which is operated by the Association of Universities for Research in Astronomy, Inc., under NASA contract NAS 5-26555. These observations are associated with programs GO-15177 and GO-13732. Some of the measurements used herein were obtained at the W. M. Keck Observatory, which is operated as a scientific partnership among the California Institute of Technology, the University of California, and the National Aeronautics and Space Administration. The observatory was made possible by the generous financial support of the W. M. Keck Foundation. The authors wish to recognize and acknowledge the very significant cultural role and reverence that the summit of Maunakea has always had within the indigenous Hawaiian community. We are most fortunate to have the opportunity to conduct observations from this mountain.

We acknowledge the use of the following software: ASTROPY (Astropy Collaboration 2013, 2018), COLOSSUS (Diemer 2018), LENSTRONOMY (Birrer & Amara 2018; Birrer et al. 2021), MATPLOTLIB (Hunter 2007), NUMPY (Walt, Colbert & Varoquaux 2011), PANDAS (McKinney 2010), PYHALO (Gilman et al. 2021), and SCIPY (Virtanen et al. 2020).

DATA AVAILABILITY

The data underlying this article will be shared on reasonable request to the corresponding author.

REFERENCES

- Afshordi N., McDonald P., Spergel D. N., 2003, *ApJ*, 594, L71
 Akeret J., Refregier A., Amara A., Seehars S., Hasner C., 2015, *J. Cosmol. Astropart. Phys.*, 2015, 043
 Astropy Collaboration, 2013, *A&A*, 558, A33
 Astropy Collaboration, 2018, *AJ*, 156, 123
 Auger M. W., Treu T., Bolton A. S., Gavazzi R., Koopmans L. V. E., Marshall P. J., Moustakas L. A., Burles S., 2010, *ApJ*, 724, 511
 Banik N., Bovy J., 2021, *MNRAS*, 504, 648
 Banik U., van den Bosch F. C., Tremmel M., More A., Despali G., More S., Vegetti S., McKean J. P., 2019, *MNRAS*, 483, 1558
 Belotsky K. M. et al., 2019, *Eur. Phys. J. C*, 79, 246
 Birrer S., Amara A., 2018, *Phys. Dark Universe*, 22, 189
 Birrer S., Amara A., Refregier A., 2017, *J. Cosmol. Astropart. Phys.*, 2017, 037
 Birrer S. et al., 2021, *J. Open Source Softw.*, 6, 3283
 Brandt T. D., 2016, *ApJ*, 824, L31
 Cai R.-G., Chen T., Wang S.-J., Yang X.-Y., 2023, *J. Cosmol. Astropart. Phys.*, 2023, 043
 Carr B. J., Hawking S. W., 1974, *MNRAS*, 168, 399
 Carr B., Kühnel F., 2020, *Annu. Rev. Nucl. Part. Sci.*, 70, 355
 Carr B. J., Sakellariadou M., 1999, *ApJ*, 516, 195
 Carr B., Silk J., 2018, *MNRAS*, 478, 3756
 Carr B., Raidal M., Tenkanen T., Vaskonen V., Veermäe H., 2017, *Phys. Rev. D*, 96, 023514
 Carr B., Clesse S., Garcia-Bellido J., Kühnel F., 2021, *Phys. Dark Universe*, 31, 100755
 Carr B., Kohri K., Sendouda Y., Yokoyama J., 2021, *Rep. Prog. Phys.*, 84, 116902
 Chapline G. F., 1975, *Nature*, 253, 251
 Chiba M., Minezaki T., Kashikawa N., Kataza H., Inoue K. T., 2005, *ApJ*, 627, 53
 Dalal N., Kochanek C. S., 2002, *ApJ*, 572, 25
 Despali G., Giocoli C., Angulo R. E., Tormen G., Sheth R. K., Baso G., Moscardini L., 2016, *MNRAS*, 456, 2486
 Diemer B., 2018, *ApJS*, 239, 35
 Dobler G., Keeton C. R., 2006, *MNRAS*, 365, 1243
 Fiacconi D., Madau P., Potter D., Stadel J., 2016, *ApJ*, 824, 144
 Gilman D., Agnello A., Treu T., Keeton C. R., Nierenberg A. M., 2017, *MNRAS*, 467, 3970
 Gilman D., Birrer S., Treu T., Nierenberg A., Benson A., 2019, *MNRAS*, 487, 5721
 Gilman D., Birrer S., Nierenberg A., Treu T., Du X., Benson A., 2020a, *MNRAS*, 491, 6077
 Gilman D., Du X., Benson A., Birrer S., Nierenberg A., Treu T., 2020b, *MNRAS*, 492, L12
 Gilman D., Bovy J., Treu T., Nierenberg A., Birrer S., Benson A., Sameie O., 2021, *MNRAS*, 507, 2432
 Gilman D., Zhong Y.-M., Bovy J., 2023, *Phys. Rev. D*, 107, 103008
 Gilman D., Benson A., Bovy J., Birrer S., Treu T., Nierenberg A., 2022, *MNRAS*, 512, 3163
 Gong J.-O., Kitajima N., 2017, *J. Cosmol. Astropart. Phys.*, 2017, 017
 Green A. M., Kavanagh B. J., 2021, *J. Phys. G: Nucl. Phys.*, 48, 043001
 Hawking S., 1971, *MNRAS*, 152, 75
 Hawkins M. R. S., 2020, *A&A*, 633, A107
 He Q. et al., 2022, *MNRAS*, 511, 3046
 Hsueh J. W., Fassnacht C. D., Vegetti S., McKean J. P., Spingola C., Auger M. W., Koopmans L. V. E., Lagattuta D. J., 2016, *MNRAS*, 463, L51
 Hsueh J. W. et al., 2017, *MNRAS*, 469, 3713
 Hsueh J. W., Enzi W., Vegetti S., Auger M. W., Fassnacht C. D., Despali G., Koopmans L. V. E., McKean J. P., 2020, *MNRAS*, 492, 3047
 Hunter J. D., 2007, *Comput. Sci. Eng.*, 9, 90
 Inoue Y., Kusenko A., 2017, *J. Cosmol. Astropart. Phys.*, 2017, 034
 Kainulainen K., Nurmi S., Schiappacasse E. D., Yanagida T. T., 2021, *Phys. Rev. D*, 104, 123033
 Khlopov M. Y., 2010, *Res. Astron. Astrophys.*, 10, 495

- Koopmans L. V. E., 2005, *MNRAS*, 363, 1136
- Laroche A., Gilman D., Li X., Bovy J., Du X., 2022, *MNRAS*, 517, 1867
- Mack K. J., Ostriker J. P., Ricotti M., 2007, *ApJ*, 665, 1277
- Mao S., Schneider P., 1998, *MNRAS*, 295, 587
- McKinney W., 2010, in van der Walt S., Millman J., eds, Proc. of the 9th Python in Sci., Conf., Data Structures for Statistical Computing in Python. Austin, Texas, p. 51
- Metcalf R. B., Madau P., 2001, *ApJ*, 563, 9
- Moustakas L. A., Metcalf R. B., 2003, *MNRAS*, 339, 607
- Müller-Sánchez F., Prieto M. A., Hicks E. K. S., Vives-Arias H., Davies R. I., Malkan M., Tacconi L. J., Genzel R., 2011, *ApJ*, 739, 69
- Murgia R., Scelfo G., Viel M., Raccanelli A., 2019, *Phys. Rev. Lett.*, 123, 071102
- Navarro J. F., Frenk C. S., White S. D. M., 1997, *ApJ*, 490, 493
- Nierenberg A. M., Treu T., Wright S. A., Fassnacht C. D., Auger M. W., 2014, *MNRAS*, 442, 2434
- Nierenberg A. M. et al., 2017, *MNRAS*, 471, 2224
- Nierenberg A. M. et al., 2020, *MNRAS*, 492, 5314
- Nierenberg A. et al., 2021, A Definitive Test of the Dark Matter Paradigm on Small Scales. JWST Proposal. Cycle 1, ID. #2046
- Oguri M., Marshall P. J., 2010, *MNRAS*, 405, 2579
- Passaglia S., Sasaki M., 2022, *Phys. Rev. D*, 105, 103530
- Planck Collaboration VI, 2020, *A&A*, 641, A6
- Quinn D. P., Wilkinson M. I., Irwin M. J., Marshall J., Koch A., Belokurov V., 2009, *MNRAS*, 396, L11
- Rubin D. B., 1984, *Ann. Stat.*, 12, 1151
- Schmidt T. et al., 2023, *MNRAS*, 518, 1260
- Shajib A. J. et al., 2022, *A&A*, 667, A123
- Sheth R. K., Mo H. J., Tormen G., 2001, *MNRAS*, 323, 1
- Sisson S. A., Fan Y., Beaumont M., 2018, Handbook of Approximate Bayesian Computation. CRC Press, New York
- Springel V. et al., 2008, *MNRAS*, 391, 1685
- Stacey H. R., McKean J. P., 2018, *MNRAS*, 481, L40
- Stacey H. R., Lafontaine A., McKean J. P., 2020, *MNRAS*, 493, 5290
- Sugai H., Kawai A., Shimono A., Hattori T., Kosugi G., Kashikawa N., Inoue K. T., Chiba M., 2007, *ApJ*, 660, 1016
- Treu T., 2010, *ARA&A*, 48, 87
- Vegetti S., Koopmans L. V. E., Bolton A., Treu T., Gavazzi R., 2010, *MNRAS*, 408, 1969
- Viel M., Becker G. D., Bolton J. S., Haehnelt M. G., 2013, *Phys. Rev. D*, 88, 043502
- Villasenor B., Robertson B., Madau P., Schneider E., 2022, Phys. Rev. D, preprint (arXiv:2209.14220)
- Virtanen P. et al., 2020, *Nat. Methods*, 17, 261
- Walt S. v. d., Colbert S. C., Varoquaux G., 2011, *Comput. Sci. Eng.*, 13, 22
- Weyant A., Schafer C., Wood-Vasey W. M., 2013, *ApJ*, 764, 116
- Wizinowich P. et al., 2022, in Schreiber L., Schmidt D., Vernet E., eds, Proc. SPIE Conf. Ser. Vol. 12185, Adaptive Optics Systems VIII. SPIE, Bellingham, p. 121850Q
- Wright S. et al., 2019, *Bull. Am. Astron. Soc.*, 51, 201
- Xu G., Ostriker J. P., 1994, *ApJ*, 437, 184
- Zel'dovich Y. B., Novikov I. D., 1967, *Sov. Astron.*, 10, 602
- Zhou H., Li Z., Liao K., Niu C., Gao H., Huang Z., Huang L., Zhang B., 2022a, *ApJ*, 928, 124
- Zhou H., Lian Y., Li Z., Cao S., Huang Z., 2022b, *MNRAS*, 513, 3627

APPENDIX: TESTING THE PIPELINE

Using 50 000 simulated lens model realizations of B1422+231, we tested the performance of our method by applying it to simulated data. We chose a realization with a low target mass and mass fraction of PBH and used the simulated flux ratios as the ‘true’ flux ratios in the computation of the summary statistic. From this, we obtain the posterior distributions shown in Fig. A1. We repeat the exercise using a high PBH mass and mass fraction, and show the resulting inference on the right of Fig. A1. The other parameters described in Section 2 were fixed in the middle of their uniform prior ranges. This process was carried out similarly for the lenses PS J1606–2333 and WGD J2038–4008, and the marginalized joint posterior distribution of all three lenses is shown in Fig. A2.

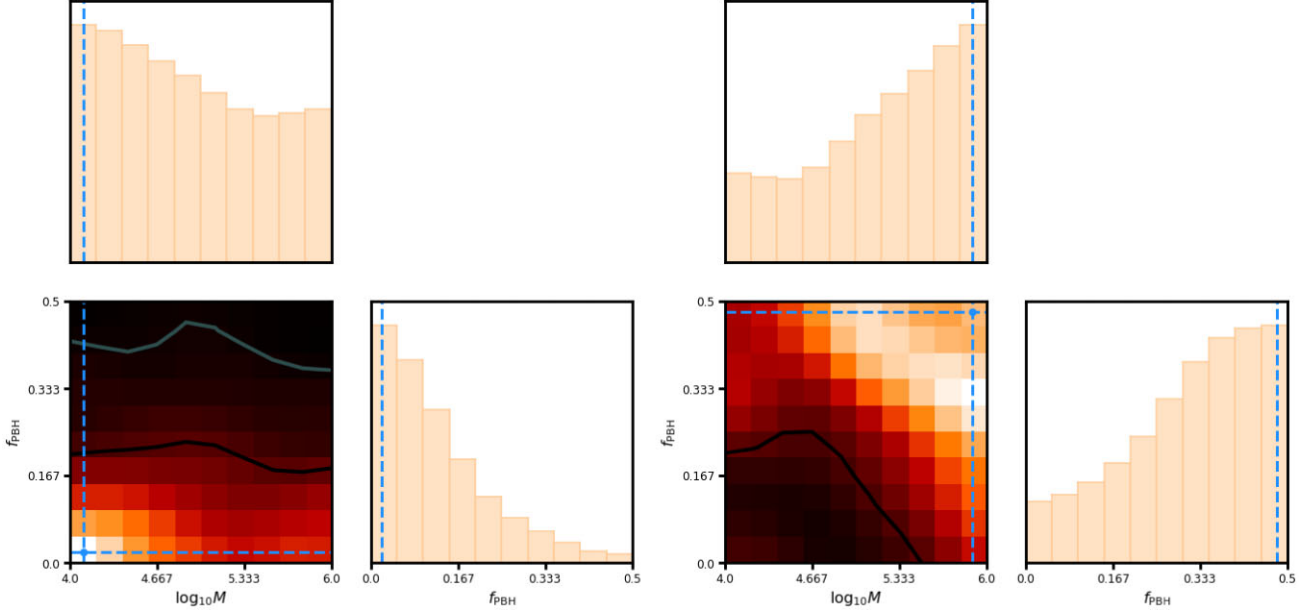


Figure A1. Posterior distributions created from simulated data using image positions and lensing priors of B1422+231. The posteriors are drawn from the 250 closest samples to the simulated ‘truth’ flux ratios represented by dashed blue lines and corresponding to $M_{\text{PBH}} = 10^{4.1} M_{\odot}$, $f_{\text{PBH}} = 0.02$ on the left and $M_{\text{PBH}} = 10^{5.9} M_{\odot}$, $f_{\text{PBH}} = 0.48$ on the right.

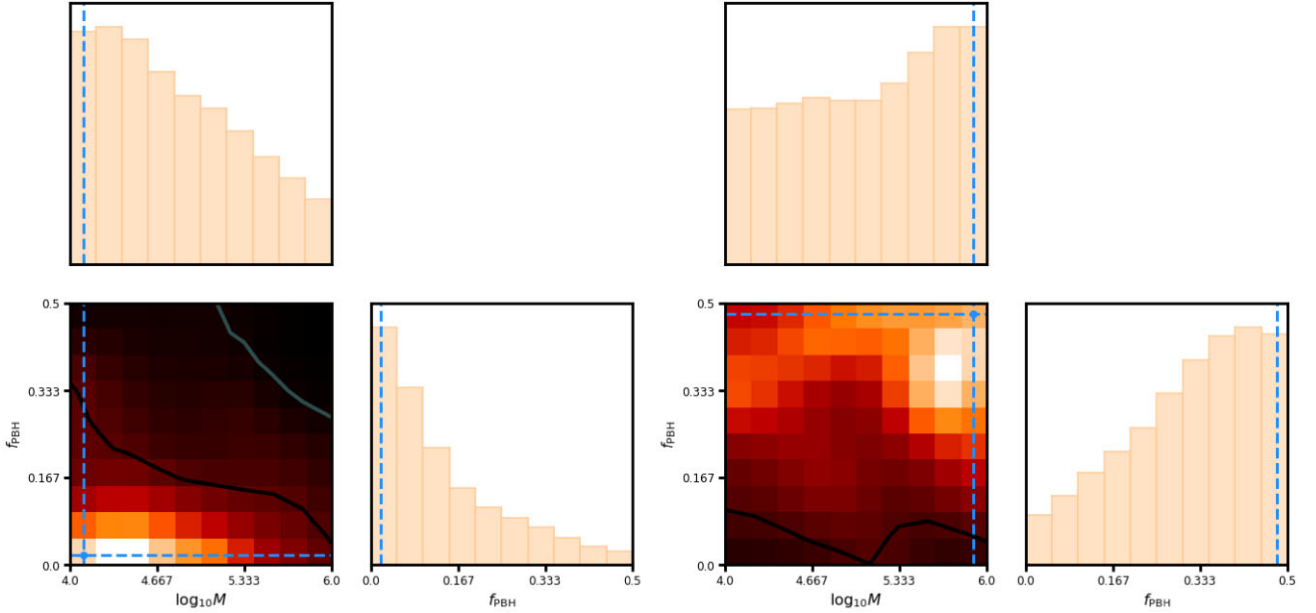


Figure A2. Product of posterior distributions based on image positions and priors of the three lenses B1422+231, PS J1606–2333, and WGD J2038–4008. As in Fig. A1, the selected ‘true’ flux ratios used to obtain each distribution are $M_{\text{PBH}} = 10^{4.1} M_{\odot}$, $f_{\text{PBH}} = 0.02$ on the left and $M_{\text{PBH}} = 10^{5.9} M_{\odot}$, $f_{\text{PBH}} = 0.48$ on the right.

This paper has been typeset from a $\text{\TeX}/\text{\LaTeX}$ file prepared by the author.